

Target and Beam-Target Spin Asymmetries in Exclusive π^+ Electroproduction for $Q^2 > 1 \text{ GeV}^2$

P.E. Bosted,³⁷ M.J. Amarian,²⁶ S. Anefalos Pereira,¹⁴ H. Avakian,³² R.A. Badui,⁹
J. Ball,⁶ N.A. Baltzell,^{32,30} M. Battaglieri,¹⁵ V. Batourine,³² I. Bedlinskiy,¹⁹ A.S. Biselli,⁸
W.J. Briscoe,¹¹ S. Bültmann,²⁶ V.D. Burkert,³² D.S. Carman,³² A. Celentano,¹⁵ S.
Chandavar,²⁵ G. Charles,¹⁸ L. Clark,³⁵ L. Colaneri,^{16,28} P.L. Cole,¹² M. Contalbrigo,¹³
V. Crede,¹⁰ A. D'Angelo,^{16,28} R. De Vita,¹⁵ A. Deur,³² E. De Sanctis,¹⁴ C. Djalali,³⁰
R. Dupre,^{18,1} H. Egiyan,^{32,23} A. El Alaoui,^{33,1,21} L. El Fassi,^{22,1} L. Elouadrhiri,³²
P. Eugenio,¹⁰ E. Fanchini,¹⁵ G. Fedotov,^{30,29} A. Filippi,¹⁷ J.A. Fleming,³⁴ T. Forest,¹²
A. Fradi,¹⁸ N. Gevorgyan,³⁸ Y. Ghandilyan,³⁸ G.P. Gilfoyle,²⁷ F.X. Girod,³² C. Gleason,³⁰
W. Gohn,^{7,*} E. Golovatch,²⁹ R.W. Gothe,³⁰ K.A. Griffioen,³⁷ M. Guidal,²¹
H. Hakobyan,^{33,38} M. Hattawy,¹ K. Hicks,²⁵ M. Holtrop,²³ S.M. Hughes,³⁴
Y. Ilieva,³⁰ D.G. Ireland,³⁵ B.S. Ishkhanov,²⁹ E.L. Isupov,²⁹ H. Jiang,³⁰ H.S. Jo,¹⁸
K. Joo,⁷ S. Joosten,³¹ G. Khachatryan,³⁸ M. Khandaker,^{12,24} A. Kim,⁷ W. Kim,²⁰
F.J. Klein,⁵ S. Koirala,²⁶ V. Kubarovsky,³² S.E. Kuhn,²⁶ L. Lanza,¹⁶ L.A. Net,³⁰
P. Lenisa,¹³ K. Livingston,³⁵ I.J.D. MacGregor,³⁵ M.E. McCracken,⁴ B. McKinnon,³⁵
C.A. Meyer,⁴ M. Mirazita,¹⁴ V.I. Mokeev,³² R.A. Montgomery,³⁵ E. Munevar,^{32,11}
C. Munoz Camacho,¹⁸ G. Murdoch,³⁵ P. Nadel-Turonski,^{32,5} S. Niccolai,¹⁸
M. Osipenko,¹⁵ A.I. Ostrovidov,¹⁰ K. Park,^{32,30} E. Pasyuk,³² P. Peng,³⁶ W. Phelps,⁹
S. Pisano,¹⁴ O. Pogorelko,¹⁹ J.W. Price,³ Y. Prok,²⁶ D. Protopopescu,³⁵ A.J.R. Puckett,⁷
B.A. Raue,^{9,32} M. Ripani,¹⁵ G. Rosner,³⁵ P. Rossi,^{32,14} R.A. Schumacher,⁴
Iu. Skorodumina,^{30,29} G.D. Smith,³⁴ D. Sokhan,³⁵ N. Sparveris,³¹ I. Stankovic,³⁴
I.I. Strakovsky,¹¹ S. Strauch,³⁰ M. Taiuti,¹⁵ B. Torayev,²⁶ M. Ungaro,^{32,7} H. Voskanyan,³⁸
E. Voutier,^{18,21} X. Wei,³² L.B. Weinstein,²⁶ J. Zhang,^{32,26} and I. Zonta^{16,28}

(The CLAS Collaboration)

¹Argonne National Laboratory, Argonne, Illinois 60439

²Arizona State University, Tempe, Arizona 85287-1504

³California State University, Dominguez Hills, Carson, CA 90747

⁴Carnegie Mellon University, Pittsburgh, Pennsylvania 15213

- ⁵*Catholic University of America, Washington, D.C. 20064*
- ⁶*CEA, Centre de Saclay, Irfu/Service de Physique Nucléaire, 91191 Gif-sur-Yvette, France*
- ⁷*University of Connecticut, Storrs, Connecticut 06269*
- ⁸*Fairfield University, Fairfield CT 06824*
- ⁹*Florida International University, Miami, Florida 33199*
- ¹⁰*Florida State University, Tallahassee, Florida 32306*
- ¹¹*The George Washington University, Washington, DC 20052*
- ¹²*Idaho State University, Pocatello, Idaho 83209*
- ¹³*INFN, Sezione di Ferrara, 44100 Ferrara, Italy*
- ¹⁴*INFN, Laboratori Nazionali di Frascati, 00044 Frascati, Italy*
- ¹⁵*INFN, Sezione di Genova, 16146 Genova, Italy*
- ¹⁶*INFN, Sezione di Roma Tor Vergata, 00133 Rome, Italy*
- ¹⁷*INFN, Sezione di Torino, 10125 Torino, Italy*
- ¹⁸*Institut de Physique Nucléaire, CNRS/IN2P3 and Université Paris Sud, Orsay, France*
- ¹⁹*Institute of Theoretical and Experimental Physics, Moscow, 117259, Russia*
- ²⁰*Kyungpook National University, Daegu 702-701, Republic of Korea*
- ²¹*LPSC, Université Grenoble-Alpes, CNRS/IN2P3, Grenoble, France*
- ²²*Mississippi State University, Mississippi State, MS 39762-5167*
- ²³*University of New Hampshire, Durham, New Hampshire 03824-3568*
- ²⁴*Norfolk State University, Norfolk, Virginia 23504*
- ²⁵*Ohio University, Athens, Ohio 45701*
- ²⁶*Old Dominion University, Norfolk, Virginia 23529*
- ²⁷*University of Richmond, Richmond, Virginia 23173*
- ²⁸*Universita' di Roma Tor Vergata, 00133 Rome Italy*
- ²⁹*Skobeltsyn Institute of Nuclear Physics, Lomonosov
Moscow State University, 119234 Moscow, Russia*
- ³⁰*University of South Carolina, Columbia, South Carolina 29208*
- ³¹*Temple University, Philadelphia, PA 19122*
- ³²*Thomas Jefferson National Accelerator Facility, Newport News, Virginia 23606*
- ³³*Universidad Técnica Federico Santa María, Casilla 110-V Valparaíso, Chile*
- ³⁴*Edinburgh University, Edinburgh EH9 3JZ, United Kingdom*
- ³⁵*University of Glasgow, Glasgow G12 8QQ, United Kingdom*

³⁶*University of Virginia, Charlottesville, Virginia 22901*

³⁷*College of William and Mary, Williamsburg, Virginia 23187-8795*

³⁸*Yerevan Physics Institute, 375036 Yerevan, Armenia*

(Dated: December 9, 2024)

Abstract

Target and beam-target spin asymmetries in exclusive π^+ electroproduction ($\gamma^*p \rightarrow n\pi^+$) were obtained from scattering of 6 GeV longitudinally polarized electrons off longitudinally polarized protons using the CEBAF Large Acceptance Spectrometer (CLAS) at Jefferson Lab. The kinematic range covered is $1.1 < W < 3$ GeV and $1 < Q^2 < 6$ GeV². Results were obtained for about 6000 bins in W , Q^2 , $\cos(\theta^*)$, and ϕ^* . Except at forward angles, very large target-spin asymmetries are observed over the entire W region. Reasonable agreement is found with phenomenological fits to previous data for $W < 1.6$ GeV, but very large differences are seen at higher W . A GPD-based model is in poor agreement with the data. When combined with cross section measurements, the present results will provide powerful constraints on nucleon resonance amplitudes at moderate and large values of Q^2 , for resonances with masses as high as 2.4 GeV.

PACS numbers: 13.60.Le, 13.88.+e, 14.20.Gk, 25.30.Rw

*Current address: University of Kentucky, LEXINGTON, KENTUCKY 40506

I. INTRODUCTION

A. Physics Motivation

Exclusive electroproduction of pseudo-scalar mesons is a process that is sensitive to the detailed internal structure of the nucleon. The process is particularly sensitive to contributions from individual nucleon resonance states. Photoproduction and electroproduction at very low four-momentum transfer squared (Q^2) continue to provide insight into the static properties of the resonances, such as mass, width, parity, spin, and decay branching ratios. Larger values of Q^2 are needed to study transition form factors, and also reveal the existence of resonances that are suppressed in photoproduction. Initial large- Q^2 measurements of spin-averaged cross sections for exclusive π^+ electroproduction from Cornell [1, 2] had limited statistical accuracy. Recent measurements from Jefferson Lab (JLab) [3–8] have greatly improved the situation.

The use of polarized nucleon targets and polarized electron beams is particularly useful in distinguishing between resonances of different spin, isospin and parity, because all single-spin asymmetries vanish in the absence of interference terms. At larger values of final-state invariant mass W , and sufficiently large values of Q^2 , the influence of nucleon resonances is thought to diminish, and the nuclear physics community has begun to describe the nucleon internal structure in terms of Generalized Parton Distributions [9, 10].

Beam asymmetries at large Q^2 for π^+n electroproduction from a proton target were published from JLab for $W < 1.7$ GeV [6] and are also the subject of an early investigation for $W > 2$ GeV [11]. Beam-target asymmetries and target single-spin asymmetries for positive and negative pions were reported from the “eg1a” and “eg1b” experiments at Jefferson Lab [12, 13] using 1.7 to 5.7 GeV electrons and a polarized ammonia target. The present experiment used 6 GeV electrons only, and greatly improves the statistical precision of exclusive positive pion electroproduction asymmetries for $Q^2 > 1$ GeV². The present analysis closely follows that presented in Ref. [13].

After a summary of the formalism, details of the experimental setup, analysis, and results are presented in the following sections.

II. FORMALISM

Because both the beam and the target were longitudinally polarized, we could, in principle, extract three spin asymmetries, defined by:

$$\sigma = \sigma_0(1 + P_B A_{LU} + P_T A_{UL} + P_B P_T A_{LL}), \quad (1)$$

where P_B and P_T are the longitudinal beam and target polarizations, respectively, σ_0 is the spin-averaged cross section, and A_{LU} , A_{UL} , and A_{LL} are the beam, target, and beam-target asymmetries, respectively. The cross sections and asymmetries are all functions of five independent variables. For this analysis, the variables $(W, Q^2, \cos(\theta^*), \phi^*, E)$ are used, where θ^*, ϕ^* are the center-of-mass decay angles of the final state with invariant mass W into a meson and a nucleon, Q^2 is the squared virtual photon four-momentum, and E is the incident electron beam energy. We use the convention that the center-of-mass final state decay polar angle $\theta^* = 0$ corresponds to a forward-going meson. The definition of ϕ^* is the opening angle between $(\vec{q} \times \vec{e})$ and $(\vec{q} \times \vec{p}_\pi)$, where \vec{e} is the incident electron momentum, \vec{q} is the momentum transfer to the scattered electron, and \vec{p}_π is the detected pion momentum.

Following the conventions of the MAID group [14], the beam and target asymmetries can be expressed as:

$$A_{LL} = -\sigma_{ez}/\sigma_0 \quad (2)$$

$$A_{UL} = \sigma_z/\sigma_0, \quad (3)$$

where

$$\begin{aligned} \sigma_{ez} = & \sqrt{2\epsilon(1-\epsilon)} [P_x \sigma_{TL'x} \cos(\phi^*) + P_y \sigma_{TL'y} \sin(\phi^*) + P_z \sigma_{TL'z} \cos(\phi^*)] + \\ & \sqrt{1-\epsilon^2} (P_x \sigma_{TT'x} + P_z \sigma_{TT'z}) \end{aligned}$$

and

$$\begin{aligned} \sigma_z = & \sqrt{2\epsilon(1+\epsilon)} (P_x \sigma_{TLx} \sin(\phi^*) + P_y \sigma_{TLy} \cos(\phi^*) + P_z \sigma_{TLz} \sin(\phi^*)) + \\ & \epsilon (P_x \sigma_{TTx} \sin(2\phi^*) + P_y \sigma_{TTy} \cos(2\phi^*) + P_z \sigma_{TTz} \sin(2\phi^*)) + P_y (\sigma_{Ty} + \epsilon \sigma_{Ly}) \end{aligned}$$

and

$$\sigma_0 = \sigma_T + \epsilon \sigma_L + \sqrt{2\epsilon(1+\epsilon)} \cos(\phi^*) \sigma_{TL} + \epsilon \cos(2\phi^*) \sigma_{TT},$$

where the direction cosines are defined as $P_z = \cos(\theta_q)$, $P_y = -\sin(\theta_q) \sin(\phi^*)$, and $P_x = \sin(\theta_q) \cos(\phi^*)$, and the virtual photon polarization as

$$\epsilon = 1/[1 + 2(1 + \nu^2/Q^2) \tan^2(\theta_e)],$$

where ν is the virtual photon energy. The angles θ_e and θ_q are relative to the beam line direction for the scattered electron and the momentum transfer, respectively. The cross sections σ_L , σ_T , σ_{TL} , σ_{TT} , $\sigma_{TL'}$, and $\sigma_{TT'}$ are functions of the three variables W , Q^2 , and θ^* , and can be evaluated from the resonance helicity amplitudes and the non-resonant Born diagrams. Although the beam asymmetry A_{LU} was measured in the present experiment, the results are not reported here, because it isn't possible to separate contributions from free and bound protons.

III. EXPERIMENT

The “eg1-dvcs” experiment [15, 16] used 6 GeV longitudinally polarized electrons from CEBAF at Jefferson Lab impinging on a 0.025 radiation length longitudinally polarized solid ammonia target immersed in liquid helium [17]. The target polarization direction is along the incident electron direction, *not* the direction of the momentum transfer vector, resulting in non-zero values of P_x and P_y . Scattered electrons and charged pions were detected in the CEBAF Large Acceptance Spectrometer (CLAS) [18]. The typical beam current was 7 nA, which, when integrated over four months of data collection with overall efficiency of 40%, resulted in approximately 2×10^{17} electrons traversing the ammonia target. The beam polarization, as periodically measured using Møller scattering in an upstream polarimeter, averaged 85%.

About 90% of the running time was on polarized protons (NH_3 target), 10% on a reference unpolarized carbon target, and 1% on an empty cell. The 1.5-cm-diameter target cups contained 1 g/cm² of material immersed in a 2-cm-long liquid helium bath. To reduce the rate of depolarization of the target from radiation damage, the sub-millimeter-diameter beam was uniformly rastered over the 1.5-cm-diameter front face of the target every few seconds. The beam position, averaged over a few minutes or longer, was kept stable at the 0.1 mm level, using feedback from a set of beam position monitors. A split solenoid superconducting magnet provided a highly uniform 5 T magnetic field surrounding the target ($\delta B/B \approx 10^{-5}$).

Particles were detected in CLAS for polar angles from 15 to 48 degrees. CLAS comprises six azimuthally symmetric detector arrays embedded in a toroidal magnetic field. Charged particle momenta and scattering angles were measured with the drift chamber tracking system. The momentum resolution ranged from about 0.5% at 0.5 GeV to over 2% at 6 GeV. The resolution in polar angles was about 1 mrad, while the azimuthal angle resolution was typically 4 mrad. Electrons were separated from a significantly larger flux of charged pions using segmented gas Cherenkov detectors (CC, pion threshold 2.6 GeV) and a sampling electromagnetic calorimeter (EC). A layer of time-of-flight scintillator counters (SC) between the CC and EC was used for hadron identification. In order to not overwhelm the data acquisition system, the hardware trigger system was designed to have high efficiency for events with a scattered electron with an energy greater than 0.3 GeV, while rejecting other events. The hardware Cherenkov and calorimeter thresholds were adjusted to give a trigger rate of about 3000 Hz, with a dead time of about 10%.

The standard CLAS detector set was augmented for this experiment with an Inner Calorimeter (IC). This calorimeter consists of an array of small lead-tungstate crystals, each 15 cm long and roughly 2 cm square. The IC is not used in the present analysis, but blocked part of the acceptance at small angle.

The data taking relevant to the present analysis was divided into two parts: Part A (early 2009) used targets centered at 58 cm upstream of the CLAS center ($z_0 = -58$ cm); Part B (mid 2009) used targets shifted 10 cm upstream to $z_0 = -68$ cm. This provided a larger acceptance for charged particles. Combined with a higher integrated luminosity, the bulk of the present results come from Part B. The CLAS torus polarity was set to bend electrons inwards for almost all of the running time, and the torus current was 2250 A. A summary of running conditions is given in Table I. Additional information about the experimental setup can be found in Refs. [15, 16].

| Run Period | Beam Energy | $P_B P_T$ | P_B |
|------------|-------------|-------------------|-----------------|
| Part A | 5.887 GeV | 0.637 ± 0.011 | 0.85 ± 0.04 |
| Part B | 5.954 GeV | 0.645 ± 0.007 | 0.85 ± 0.04 |

TABLE I: Run period names, nominal beam energy, $P_B P_T$ and P_B , where P_B (P_T) is the beam (target) polarization, for the two running periods of the experiment.

IV. ANALYSIS

A. Data Processing

A subset of the data was used to calibrate the response of all of the CLAS detectors and instruments used to measure beam position and current. The alignment of the detectors, as well as the target magnet, were also determined.

The raw data were passed through a standard CLAS analysis package that transformed raw timing and pulse-height signals into a set of “particles” for each trigger event. Direction cosines at the target for charged particles, as well as their momenta, were determined from their tracks as measured by the drift chambers (DC). For neutron candidates, direction cosines were determined from their hit positions in the EC. Charged-particle tracks were associated with the corresponding CC signals, EC energy deposition, and timing from the SC using geometrical matching. Additional details can be found in the two archival papers describing the eg1b inclusive analysis [19, 20].

A subset of the recorded events was subsequently written to skimmed data files for further processing. These data files only contained events that had a reasonable chance of passing the event selection cuts of the present analysis.

B. Particle Identification

We analyzed π^+ electroproduction using two topologies: $ep \rightarrow e\pi^+n$ and $ep \rightarrow e\pi^+(n)$. Both topologies require detection of the scattered electron and a pion. The $ep \rightarrow e\pi^+n$ topology also requires the detection of a neutron. The total number of events passing the cuts of topology $ep \rightarrow e\pi^+n$ was 32438 for Part A, and 96215 for Part B. The total number of events passing the cuts of topology $ep \rightarrow e\pi^+(n)$ was 208835 for Part A, and 684981 for Part B.

1. Electron identification

Electrons were identified by requiring a signal of at least one photo-electron in the Cherenkov detector, at least two thirds of the most probable electron energy to be deposited in the EC, and a vertex position reconstructed within 4 cm of the nominal target

center. The electron scattering angle was required to be between 15.5 and 38 degrees. These cuts are not as restrictive as those placed on electrons for the inclusive electron scattering analysis [15] of the present experiment, because the exclusivity cuts discussed below remove essentially all of the events where a pion might be mis-identified as an electron.

2. *Charged Pion Identification*

Charged pions were identified by requiring that the time-of-arrival at the scintillator counters be within 0.7 ns of that predicted from the time-of-arrival of the electron in the event. This timing cut removed all protons from the sample, but allowed between 10% to 100% of K^+ , depending on kaon momentum. These events were removed by the missing mass cut discussed below. Positrons were removed from the sample by requiring small (or no) signal in the Cherenkov detector and a small deposited energy in the electromagnetic calorimeter. Also required were a vertex position reconstructed within 4 cm of the nominal target center, and a polar scattering angle between 15 and 48 degrees.

3. *Neutron Identification*

Neutrons were identified by requiring a deposited energy of at least 0.3 GeV in the EC, with a time-of-arrival at the EC corresponding to $\beta < 0.95$ to separate neutrons and photons. The direction cosines of the neutron were determined from the EC hit coordinates. In some cases, the neutrons passed through the Inner Calorimeter on the way to the EC. Generally, this had no effect on the neutrons, because the number of interactions lengths in the IC was relatively small. In the case where the neutron interacted in the IC, making a hadronic shower, the exclusivity cuts on direction cosines removed most of these events, effectively further lowering the already low neutron detection efficiency. The neutron momentum could not be determined from time-of-flight with sufficient accuracy to be useful.

C. **Exclusivity Kinematic Cuts**

For both topologies, kinematic cuts were placed to improve the signal to noise ratio. The value of kinematic cuts is two-fold. First, most of the kinematic quantities have a wider

distribution for bound nucleons (in target materials with $A > 2$) than for free protons. Kinematic cuts therefore reduce the dilution of the signal of interest (scattering from polarized free protons) compared to the background from unpolarized nucleons in materials with $A > 2$. Second, kinematic cuts are needed to isolate single meson production from multi-meson production.

For the $ep \rightarrow e\pi^+(n)$ topology, the only kinematic cut available is on the missing mass. For the $ep \rightarrow e\pi^+n$ topology, cuts on the cone angles of the detected neutron further reduce nuclear backgrounds.

1. *Electron-pion Missing Mass Cut*

For both topologies, the electron-pion missing mass $M_x^{e\pi}$ should be equal to the neutron mass of 0.939 GeV. In general, one would like the upper cut on $M_x^{e\pi}$ to be well below $M + m_\pi = 1.08$ GeV, to avoid contributions from multi-pion production. Placing tighter cuts helps to reduce the nuclear background.

The distribution in $M_x^{e\pi}$ is shown for topology $ep \rightarrow e\pi^+(n)$ in Fig. 1 averaged over the full kinematic range of the experiment. The solid circles correspond to counts from the ammonia target, while the open circles correspond to counts from the carbon target, scaled by the ratio of luminosities on $A > 2$ nucleons. A clear peak is seen near the nucleon mass from the ammonia target, with a smaller but wider distribution from the carbon target, that matches the wings on the ammonia distributions on the low-mass side of the peak. On the high side of the peak, the ammonia rates are higher, due to the radiative tail of the single-pion production, and the gradual turn-on of multi-pion production. The vertical dashed lines show the cuts used: $0.86 < M_x^{e\pi} < 1.02$ GeV. Within the cut region, approximately half of the events come from nucleons in nuclei with $A > 2$, and half from free protons.

The distribution in $M_x^{e\pi}$ is shown for topology $ep \rightarrow e\pi^+n$ in Fig. 2. The nuclear background is greatly reduced in this case, because additional cuts can be placed on the direction cosines of the detected neutron.

The spectra were examined to see if the optimal cut value depends on W , Q^2 , $\cos(\theta^*)$, or ϕ^* . Although the peak widths vary somewhat with kinematic variables, a constant cut value did not degrade the signal to noise ratios by more than a few percent.

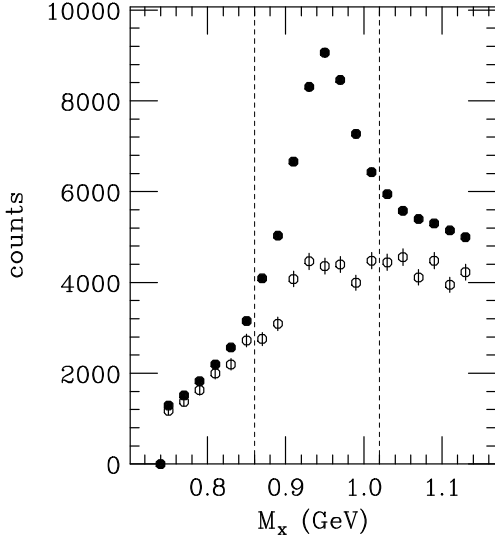


FIG. 1: Electron-pion missing mass spectra for the topology $ep \rightarrow e\pi^+(n)$. Counts from the ammonia target are shown as the solid circles and counts from the carbon target (scaled by the ratio of integrated luminosities on bound nucleons) are shown as the open circles. The vertical dashed lines indicate the cuts used.

2. Neutron Angular Cuts

In the topology $ep \rightarrow e\pi^+n$, cuts on the cone angles of the neutron are very useful in rejecting background from $A > 2$ materials. From the kinematics of the detected electron and pion, the direction cosines of the recoil neutron are calculated, and compared with the observed angles. We denote the difference in predicted and observed angles as $\delta\theta_N$ in the in-plane direction and $\delta\phi_N$ in the out-of-plane direction (which tends to have worse experimental resolution). Distributions of these two quantities are shown in Figs. 3 and 4,

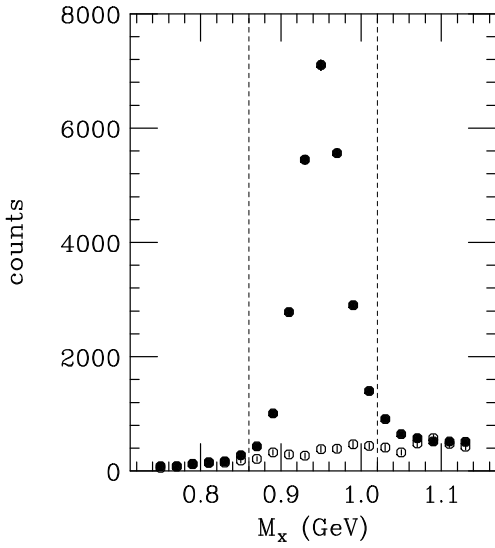


FIG. 2: Same as Fig. 1, but for the topology $ep \rightarrow e\pi^+n$. Cuts on the neutron angle have been applied.

respectively. It can be seen that with cuts on M_x and the complementary angle, the nuclear background is relatively small and flat compared to the peaks from the free proton. We used the cuts $\|\delta\theta_N\| < 3^\circ$ and $\|\delta\phi_N\| < 6^\circ$, for all kinematic bins. Events that failed either one of these cuts were not moved over to the $ep \rightarrow e\pi^+(n)$ topology event sample.

D. Kinematic Binning

The kinematic range of the experiment is $1.1 < W < 3$ GeV and $1 < Q^2 < 6$ GeV². As shown in Fig. 5, the range in Q^2 changes with W . We therefore made four bins in Q^2 , where the limits correspond to electron scattering angles of 15.5, 18, 21, 26, and 38 degrees.

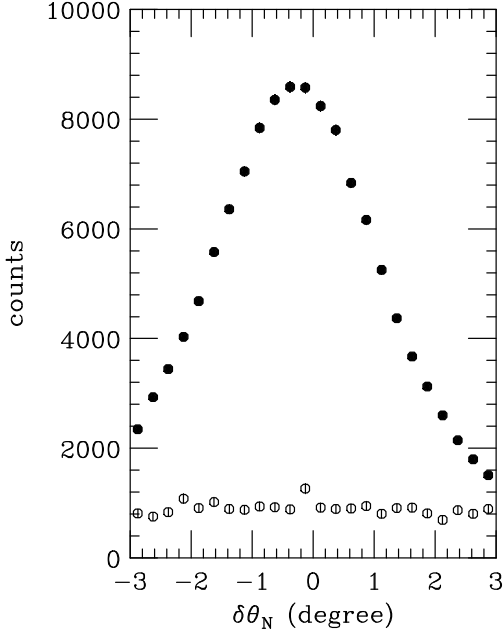


FIG. 3: Distribution of the in-plane angular difference in predicted and observed nucleon direction cosines for the topology $ep \rightarrow e\pi^+n$. The black points are for the ammonia target, while the open circles are from the carbon target, scaled by integrated luminosity. The analysis cuts correspond to the edge of the histogram. All other relevant exclusivity cuts (i.e. on $M_x^{e\pi}$ and $\delta\phi_N$) have been applied.

In order to study possible resonance structure, we used fixed W bins of width 0.05 GeV for $W < 2$ GeV, which is comparable to the experimental resolution. For $W > 1.9$ GeV, the bin widths gradually increase, to achieve roughly equal counting rates, with bin boundaries at 1.90, 1.96, 2.03, 2.11, 2.20, 2.31, 2.43, 2.56, 2.70, 2.85 and 3 GeV. The bin limits are shown in Fig. 5.

An examination of event rates showed a strong forward peaking in $\cos(\theta^*)$ for both

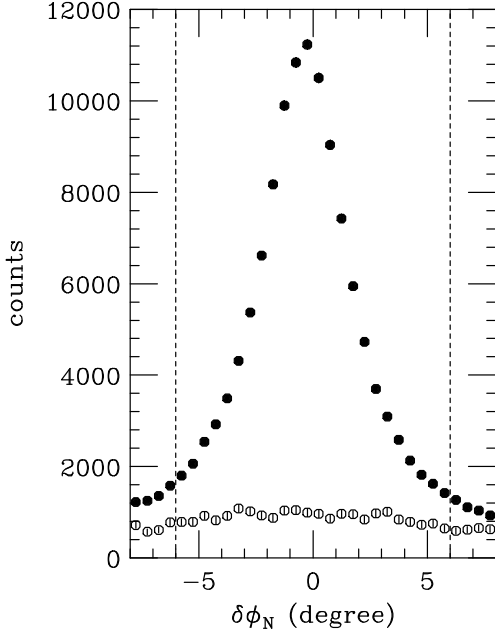


FIG. 4: Same as Fig. 3, except now for the out-of-plane angular difference (after application of cuts on $M_x^{e\pi}$ and $\delta\theta_N$) The vertical dashed lines indicate the cuts used in the analysis.

topologies studied, roughly independent of (W, Q^2) . There are essentially no events with $\cos(\theta^*) < -0.2$. We decided to use six bins in $\cos(\theta^*)$, with boundaries at -0.2, 0.2, 0.44, 0.63, 0.78, 0.9, and 0.995. The upper-most boundary of 0.995 was chosen instead of 1.0 because the average resolution in ϕ^* becomes larger than 30 degrees above $\cos(\theta^*) = 0.995$, making it increasingly problematic to determine the ϕ^* -dependence of the spin asymmetries at very forward angles. We used 12 bins in ϕ^* , equally spaced between 0 and 2π .

A strong consideration in choosing the bin sizes was that we required at least ten counts in a given bin in order to have Gaussian statistical uncertainties. The total number of bins is 7488, of which about 6000 had enough events to be included in the final results.

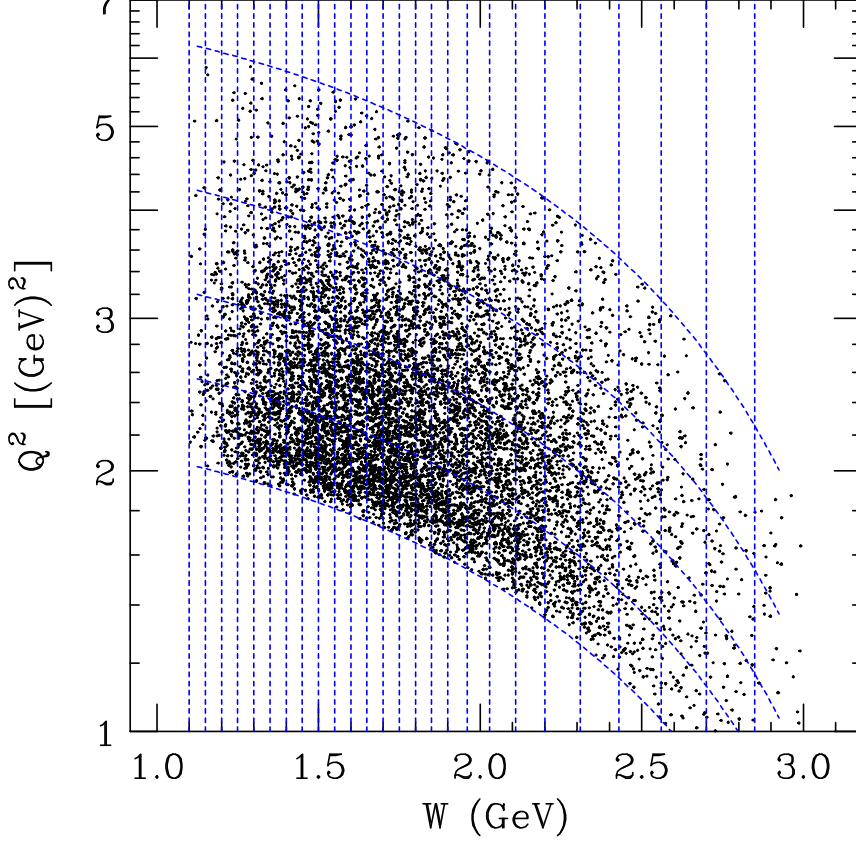


FIG. 5: Distribution in (W, Q^2) of events for the $ep \rightarrow e\pi^+(n)$ topology passing all exclusivity cuts. The vertical dashed lines show the limits of the W bins used in the analysis, while the left-to-right curves show the bin limits in Q^2 , defined by fixed bins in θ_e of 15.5, 18, 21, 26, and 38 degrees (from bottom to top).

V. ASYMMETRIES

Spin asymmetries were formed as follows:

$$A_{LL} = \frac{N^{\uparrow\downarrow} + N^{\downarrow\uparrow} - N^{\uparrow\uparrow} - N^{\downarrow\downarrow}}{N_{tot} f P_B P_T}, \quad (4)$$

$$A_{UL} = \frac{N^{\uparrow\uparrow} + N^{\downarrow\downarrow} - N^{\uparrow\downarrow} - N^{\downarrow\uparrow}}{N_{tot} f P_T}, \quad (5)$$

where the symbols N represent the number of events in a given helicity configuration, divided by the corresponding integrated beam current. The first superscript refers to the beam

polarization direction, and the second to the target polarization direction. The total number of counts is denoted by $N_{tot} = N^{\uparrow\uparrow} + N^{\downarrow\uparrow} + N^{\uparrow\downarrow} + N^{\downarrow\downarrow}$, and f is the dilution factor, defined as the fraction of events originating from polarized free protons, compared to the total number of events.

A. Beam and Target Polarization

The product of beam polarization (P_B) and target polarization (P_T) was determined using the well-understood beam-target spin asymmetry in elastic ep scattering. The results are listed in Table I. The beam polarization was measured using Møller scattering, and are also listed in the table. The proton target polarization was determined by dividing $P_B P_T$ by P_B . This proved to be more accurate than using direct NMR measurements of the target polarization, which were relatively accurate from run-to-run, but had a large overall normalization uncertainty.

B. Dilution Factor

The dilution factor f is defined as the ratio of scattering rate from free nucleons to the scattering rate from all nucleons in the target. With the assumption that the cross section per nucleon is the same for bound protons in all of the nuclear materials (with $A > 2$) in a given target, and also that the effective detection efficiency is the same for the ammonia and carbon targets, then

$$f = 1 - R_{A>2} \frac{N_C}{N_{NH_3}}, \quad (6)$$

where N_C and N_{NH_3} are the number of counts from the carbon and ammonia targets respectively, measured in a given kinematic bin for a given topology, normalized by the corresponding integrated beam charge. The symbol $R_{A>2}$ denotes the ratio of the number of bound nucleons in the ammonia target to the number of bound nucleons in the carbon target. Bound nucleons are defined to be in materials with atomic number $A > 2$. The latter was determined from a detailed analysis of the target composition using inclusive electron scattering rates from ammonia, carbon, and empty targets, yielding $R_{A>2} = 0.71$ for Part A and $R_{A>2} = 0.72$ for Part B.

Because the integrated luminosity on the carbon target was about ten times lower than

on the ammonia target, there is a large amplification of the uncertainty on the ratio of carbon to ammonia counts, $\frac{N_C}{N_{NH_3}}$. In many cases, this would lead to unphysical values of f (i.e. $f < 0$). We therefore took advantage of the fact that f is a very slowly varying function of kinematic variables, and did a global fit to $\frac{N_C}{N_{NH_3}}$. The fit values were then used to evaluate f in each kinematic bin.

As in Ref. [13], the functional forms for the fit contained 25 terms of the form $p_i \cos^{N_C}(\theta^*) W^{N_W} (Q^2)^{N_Q}$, where p_i is a free parameter, and the exponents N_C , N_W , and N_Q range from 0 to 3 (although not all possible terms were included). An additional eight terms were included to account for the influence of the three prominent nucleon resonances centered at 1.23 GeV, 1.53 GeV, and 1.69 GeV, with widths 0.220 GeV, 0.120 GeV, and 0.120 GeV. The reason that these resonance terms are needed is that the nucleon resonances are effectively broadened in the target materials with $A > 2$ by Fermi motion. This generates resonant-like structures in the ratio of carbon to ammonia count rates. Tests were made to see if any ϕ^* -dependent terms would improve the fits. No significant improvements were found.

The dilution factors for Part B for the two topologies are shown in Fig. 6 as a function of W for the four Q^2 bins of this analysis and a typical bin in $\cos(\theta^*)$. For the fully exclusive topology, $ep \rightarrow e\pi^+n$, the dilution factor is large, about 0.8 on average, corresponding to the good rejection of background that is possible with the exclusivity cuts when the recoil neutron is detected. For the topology $ep \rightarrow e\pi^+(n)$, the dilution factor is reasonably good for $W < 2$ GeV, averaging about 0.45, with significant resonant structure visible. For $W > 2$ GeV, there is a trend for f to decrease, dropping to values as low as 0.25 at the highest values of W . This is because Fermi broadening results in an increasing amount of multi-pion production from the nuclear target material. The Q^2 -dependence is relatively weak for both topologies. Because Part A had much lower statistical accuracy than Part B, we used the Part B fits for Part A.

C. Combining Data Sets

The entire asymmetry analysis was performed separately for Part A and Part B. The results were combined by averaging asymmetries, weighted by their respective statistical uncertainties, for each of the 4-dimensional bins. Since the two configurations differ only in

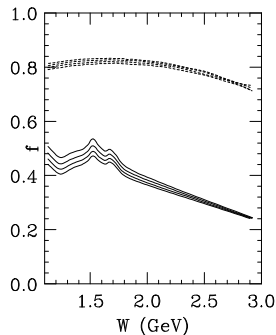


FIG. 6: Dilution factors as a function of W for the $ep \rightarrow e\pi^+n$ topology (dashed curves) and the $ep \rightarrow e\pi^+(n)$ topology (solid curves) for the four Q^2 bins of this experiment and a typical bin in $\cos(\theta^*)$.

the acceptance function, which should cancel in forming the asymmetries, the expectation is that they should be fully compatible statistically. This was verified by forming the χ^2 per degree of freedom for combining each of the asymmetries for both topologies.

D. Combining Topologies

We next combined the fully exclusive topology with the one with a missing neutron. For both asymmetries, the topologies were found to be statistically compatible. This good agreement between topologies can be observed by visual examination of plots in which both topologies are plotted together, such as Fig. 7, which show A_{LL} for the two π^+ topologies as a function of W in a grid over θ_e (i.e. Q^2) and $\cos(\theta^*)$. In this figure, adjacent bins in W were averaged together, and a straight average over ϕ^* was performed.

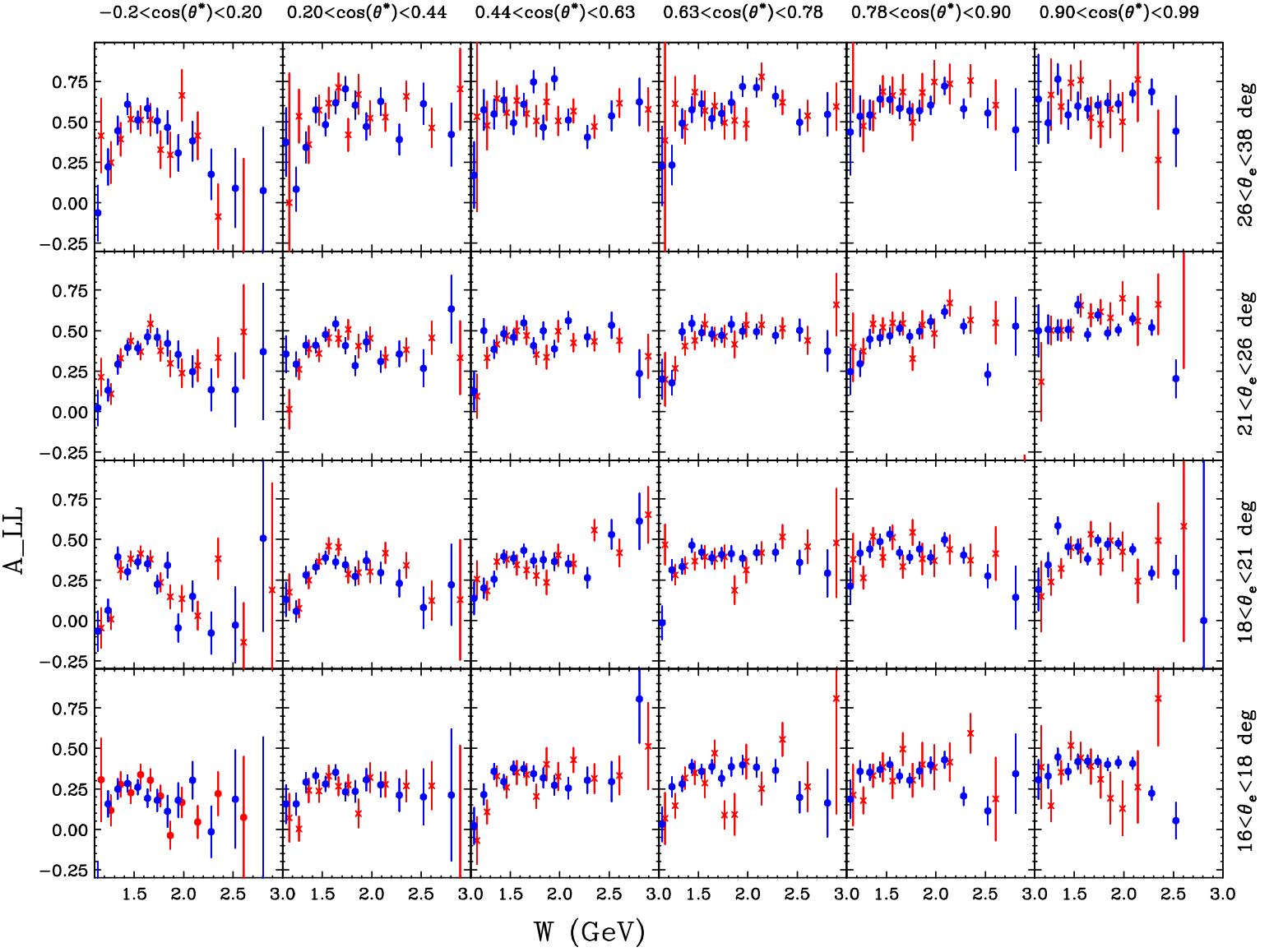


FIG. 7: (color online) Beam-target double spin asymmetry A_{LL} for the $ep \rightarrow e\pi^+n$ topology (red crosses) compared to the $ep \rightarrow e\pi^+(n)$ topology (blue circles), averaged over ϕ^* , as a function of W , in the six $\cos(\theta^*)$ bins of this analysis and the four Q^2 (θ_e) bins used.

E. Radiative Corrections

Radiative corrections take into account that the incident beam energy, scattered electron energy, or the electron scattering angle at the vertex can all be different from those measured in the detector, due to electrons radiating photons in the field of a nucleon or nucleus. Although the corrections are significant for spin-averaged exclusive cross sections, they are negligible for spin asymmetries, due to the facts that Bremsstrahlung is largely spin-independent, and the cross section variation is small within the exclusivity cuts used for a given kinematic bin. This was verified by explicit calculations using the Mo-Tsai formalism [21] with the equivalent radiator approximation (internal radiation equivalent to external radiation) and the angle peaking approximation (photon emitted along the incident or scattered electron direction only). In these calculations, we used the MAID fit [14] to describe the cross section and asymmetry variations within each kinematic bin. The calculations were performed using a Monte Carlo simulation technique. Within the statistical error of the calculation (typically $\delta A = 0.005$ for a given kinematic bin), no significant deviations from zero were observed. The average depolarization of the electron from Bremsstrahlung was also evaluated, and found to be much less than 1%.

F. Polarized Nitrogen Correction

As is discussed in Ref. [15], the nitrogen in the ammonia targets is slightly polarized, and in the case of inclusive electron scattering, a correction of about 1.8% to the beam-target asymmetry is needed. In the present exclusive analysis, the correction is reduced to about 0.5% for $ep \rightarrow e\pi^+(n)$ and less than 0.2% for $ep \rightarrow e\pi^+n$, because most of the events from nitrogen are removed by the exclusivity cuts. No corrections were applied in the present analysis, and this omission is accounted for in the systematic uncertainty budget.

G. Systematic uncertainties

The dominant systematic uncertainty on all the asymmetry results is an overall scale uncertainty from the beam and target polarizations. The uncertainty in A_{LL} is relatively small (1.4%) because $P_B P_T$ was well-measured using ep elastic scattering. The relative uncertainty in A_{UL} is larger (4%) due to the uncertainty in P_B , from which we obtained P_T

by dividing $P_B P_T$ by P_B .

The other source of normalization uncertainty is the dilution factor. As discussed in more detail in Ref. [15], the uncertainties in the target composition correspond to about a 2.5% relative uncertainty in the amount of background subtraction, which corresponds to 1% to 1.5% in the asymmetry results, for the missing neutron topology, and less than 0.5% for the fully exclusive topology.

Another source of systematic uncertainty is in the factor $R_{A>2}$. We compared three methods of determining this factor: a study of inclusive electron scattering rates; fits to the low electron-pion missing mass spectra; and the value that gives the best agreement for A_{LL} between the fully exclusive topology and the topology where the recoil nucleon is not detected. This last technique relies on the fact that the fully exclusive topology has much less nuclear background. From these comparisons, we estimate a systematic uncertainty of about 2% (relative) for $R_{A>2}$. This translates into approximately 1.5% (at low W) to 2.5% (at high W) overall normalization uncertainties on both A_{LL} and A_{UL} .

It is also possible for assumptions made in the dilution factor fitting, such as the lack of ϕ^* dependence, to result in point-to-point systematic uncertainties. Based on trying out several different functional forms to the fit, these were found to be much smaller than the point-to-point statistical uncertainties.

Finally, it is clear from Fig. 1 that the cut on electron-pion missing mass is not 100% effective at removing multi-pion production, for the topology with one missing nucleon. Since the contamination is larger for $M_x^{e\pi} > M$ than for $M_x^{e\pi} < M$, we divided the data into two distinct sets, based on the above criteria, and compared both A_{LL} and A_{UL} asymmetries. We obtained $\chi^2/\text{d.f.}=0.98$ ($\chi^2/\text{d.f.}=1.02$) for agreement of the two A_{LL} (A_{UL}) data sets, indicating that the admixture of some multi-pion events into the single pion samples does not affect the final asymmetry results significantly.

Adding the above sources of uncertainty in quadrature, we obtain overall normalization uncertainty of 3% for A_{LL} and 5% for A_{UL} .

VI. RESULTS

With over 7000 kinematic points, each with relatively large uncertainties, it is a challenge to portray the entire data set in a meaningful way. For plotting purposes, we therefore

averaged together adjacent bin triplets or quartets in W , and adjacent bin pairs in Q^2 . The complete set of results is available in the CLAS data base [22] and in the Supplemental Material associated with this article [23]. All results are for the fully exclusive topology and the topology with a missing neutron combined together, as explained above.

A. A_{LL}

The results for the beam-target spin asymmetry A_{LL} are plotted as a function of ϕ^* in seven bins in W and six bins in $\cos(\theta^*)$ in Fig. 8 for the lower Q^2 data and in Fig. 9 for the higher Q^2 data. There is very little difference between these plots, indicating a weak dependence on Q^2 for a given kinematic bin.

The main feature of the data is a relatively large and positive asymmetry (averaging about 0.4) for most kinematic bins. The major exception is for the lowest W bin, centered on the $\Delta(1232)$ resonance, where the values of A_{LL} are closer to zero. This feature is expected because the $\Delta(1232)$ transition is dominated by spin-1/2 to spin-3/2, which gives a negative value of A_{LL} , balancing the positive contribution from the Born terms. Of particular interest are the bins centered on $W = 1.70$, $W = 1.91$ and $W = 2.19$ GeV. Here, A_{LL} is roughly 0.4, independent of ϕ^* , at forward angles where t -channel processes dominate. At lower values of $\cos(\theta^*)$, an increasingly large ϕ^* -dependence can be seen, with a noticeable enhancement near $\phi^* = 180^\circ$. This suggests the importance of s -channel resonance excitations.

Also shown on the plots are the results of two representative fits to previous data (limited to $W < 2$ GeV): the 2007 version of the MAID unitary isobar fit [14] and the Unitary Isobar version of the JLab Analysis of Nucleon Resonances (JANR) fit [24], averaged with the same weighting as the data points. Formally, these two fits are rather similar in nature, but differ in the data sets used, and in the functional forms used for the Q^2 -dependence of the resonance form factors. By and large, both the MAID 2007 and the JANR fits describe the data reasonably well up to $W = 1.6$ GeV, with large differences in the ϕ^* -dependence appearing at larger W . Also shown on the plots are the GPD-based model of Goloskokov and Kroll [10], which has no explicit s -channel resonance structure included. This model is generally predicts larger values of A_{LL} than observed.

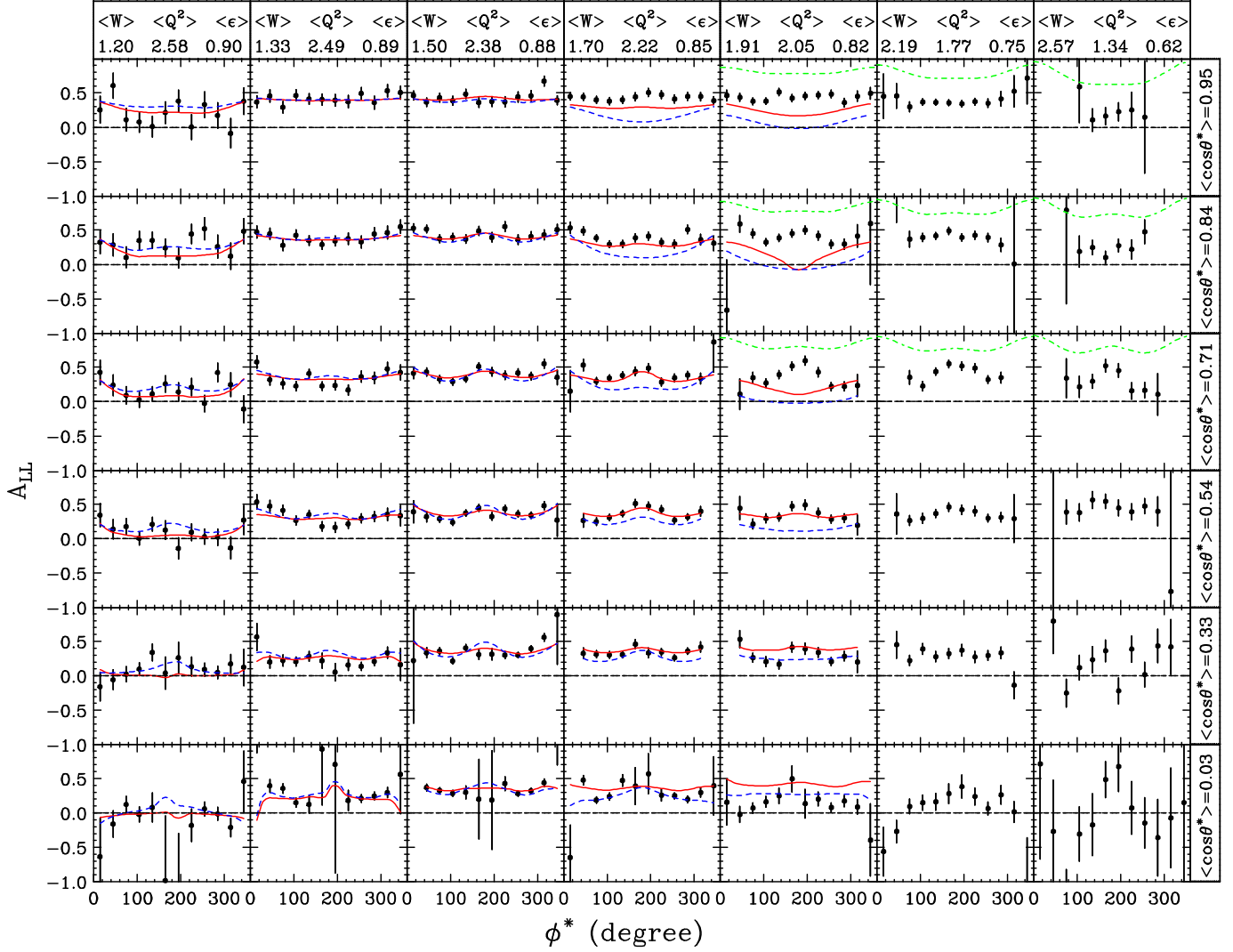


FIG. 8: (color online) Beam-target double spin asymmetry A_{LL} for the reaction $ep \rightarrow e\pi^+n$ as a function of ϕ^* in seven bins in W (rows) and six $\cos(\theta^*)$ bins (columns). The results are from the two lower Q^2 bins of this analysis. The error bars reflect statistical uncertainties only. The solid red curves are from the MAID 2007 fit [14], the blue long-dashed curves are from a JANR fit [24], and the green short-dashed curves are for the GPD-inspired model from Goloskokov and Kroll [10].

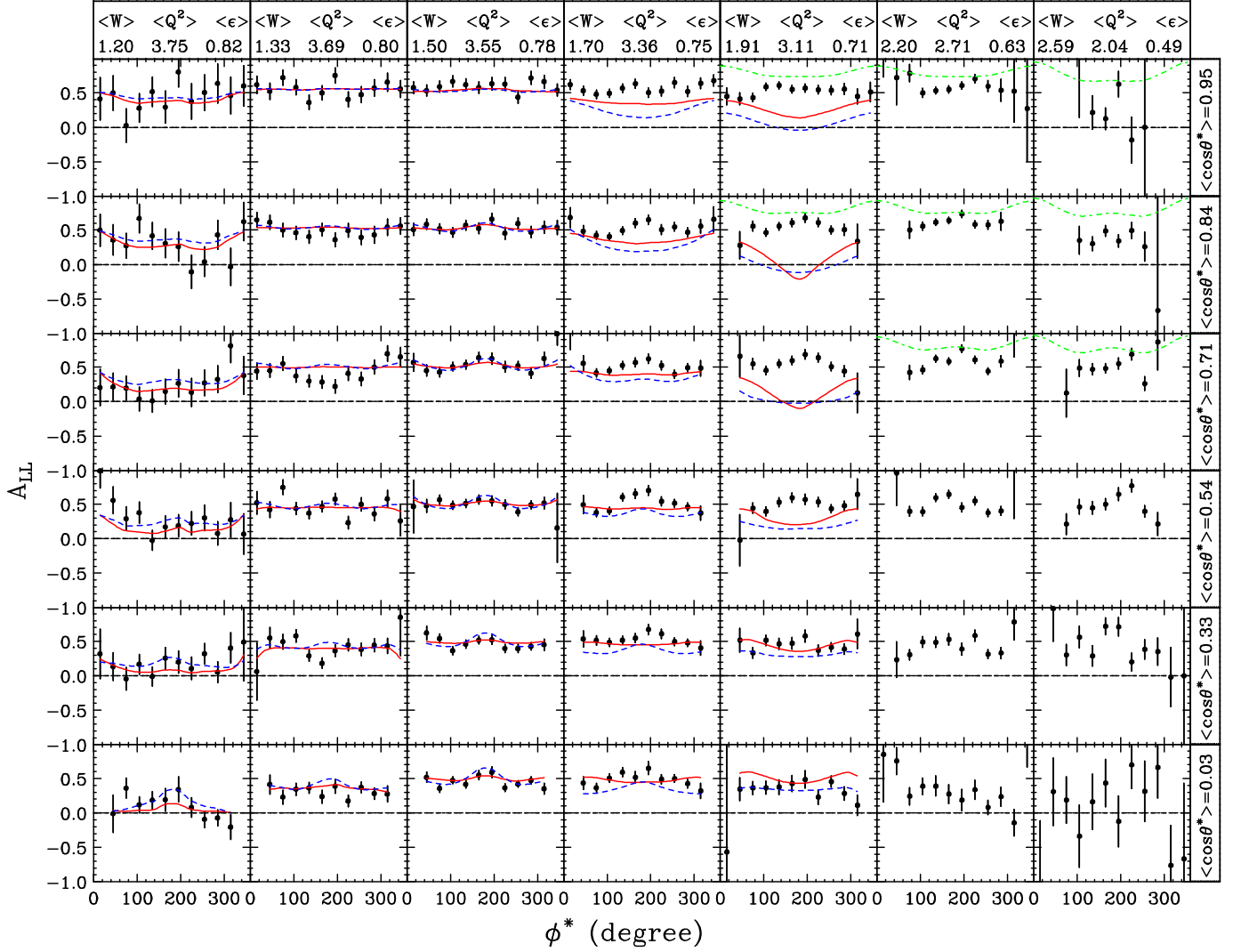


FIG. 9: Same as Fig. 8, except for the two larger Q^2 bins of this analysis.

B. A_{UL}

The results for the target spin asymmetry A_{UL} are plotted as a function of ϕ^* in seven bins in W and six bins in $\cos(\theta^*)$ in Fig. 10 for the lower Q^2 data, and in Fig. 11 for the higher Q^2 data. It can be seen that the Q^2 -dependence of the results is weak. The main feature of the data is a positive $\sin(\phi^*)$ modulation that is small at forward angles, and grows to nearly maximal values at central angles, even at the largest values of W .

The sign and magnitude of this modulation is well reproduced by the MAID and JANR fits for $W < 1.4$ GeV, where the $\Delta(1232)$ resonance dominates. At larger values of W , both fits predict a sign change in the $\sin(\phi^*)$ modulation, which is not observed in the data. The magnitude of the modulation is also much larger in the data than in the models near $\cos(\theta^*) = 0$. The GPD-inspired model from Goloskokov and Kroll [10] agrees well with the small asymmetries observed at very forward angles, but does not predict the large asymmetries observed at smaller values of $\cos(\theta^*)$.

Combined with the results for A_{LL} , the results for A_{UL} strongly suggest that there are important nucleon resonance contributions to exclusive pion electroproduction for $W > 1.6$ GeV and $Q^2 > 1$ GeV². For example, the Particle Data Group [25] lists four “3-star” and “4-star” N^* resonances with masses above 2 GeV (at 2190, 2220, 2250, and 2600 MeV) and a “4-star” Δ resonance with mass 2420 MeV.

VII. SUMMARY

Target and beam-target spin asymmetries in exclusive π^+ electroproduction ($\gamma^*p \rightarrow n\pi^+$) were obtained from scattering of 6 GeV longitudinally polarized electrons from longitudinally polarized protons using the CLAS detector at Jefferson Lab. The kinematic range covered is $1.1 < W < 3$ GeV and $1 < Q^2 < 6$ GeV². Results were obtained for about 6000 bins in W , Q^2 , $\cos(\theta^*)$, and ϕ^* . Except at forward angles, very large target-spin asymmetries are observed over the entire W region. Reasonable agreement is found with the phenomenological MAID 2007 fit [14] and the JANR fit [24] to previous data for $W < 1.5$ GeV, but very large differences are seen at higher values of W , where no large- Q^2 data were available when the fits were made. The large target-spin asymmetries are also not accounted for by a GPD model. We anticipate that the present target and beam-target asymmetry data, when combined with beam-spin asymmetry and spin-averaged cross section data in new global analyses, will yield major insights into the structure of the proton and its many excited states.

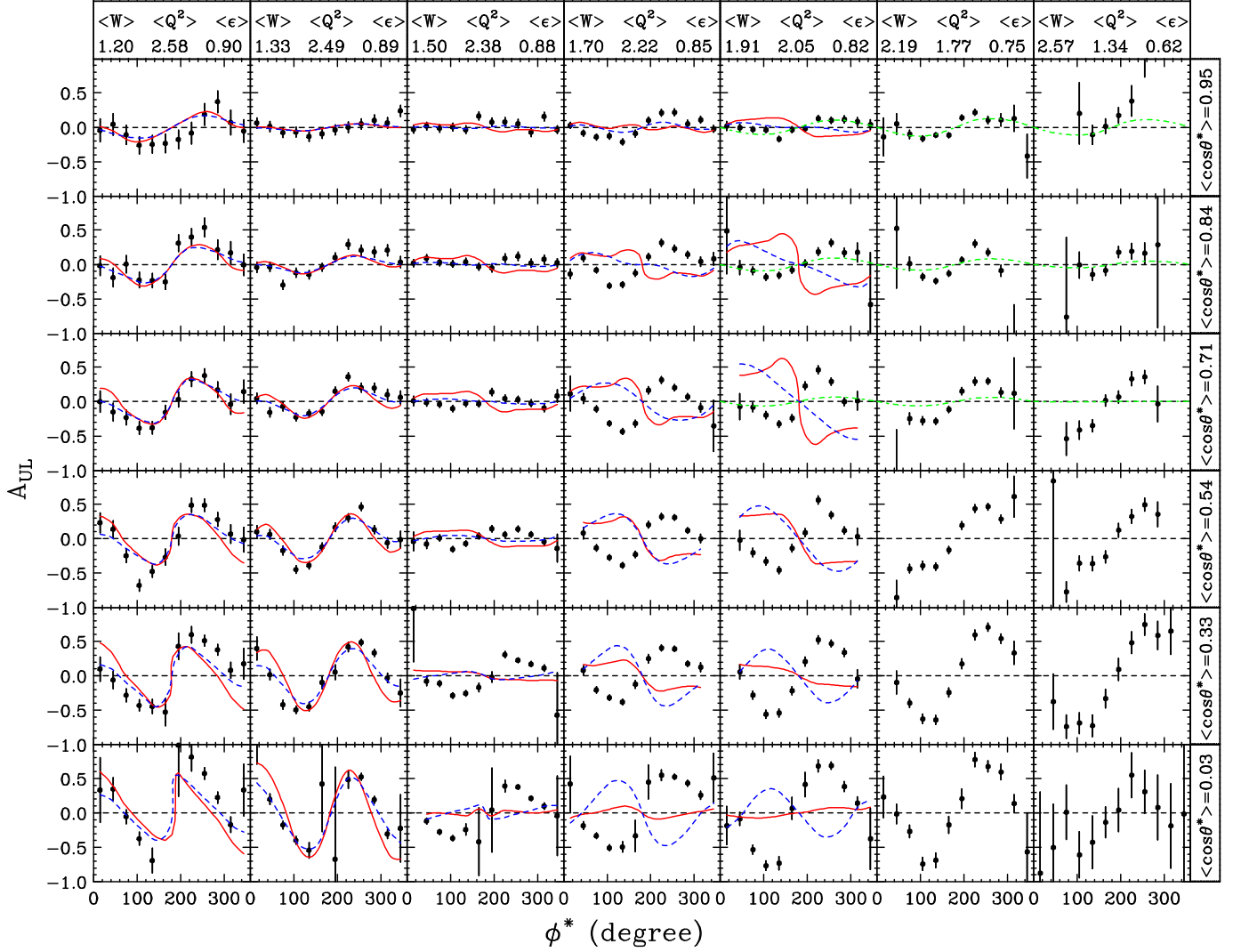


FIG. 10: Target single-spin asymmetry A_{UL} for the reaction $ep \rightarrow e\pi^+n$ as a function of ϕ^* in seven bins in W (rows) and six $\cos(\theta^*)$ bins (columns). The results are from the two lower Q^2 bins of this analysis. The error bars reflect statistical uncertainties only. The solid red curves are from the MAID 2007 fit [14], the blue long-dashed curves are from a JANR fit [24], and the green short-dashed curves are for the GPD-inspired model from Goloskokov and Kroll [10].

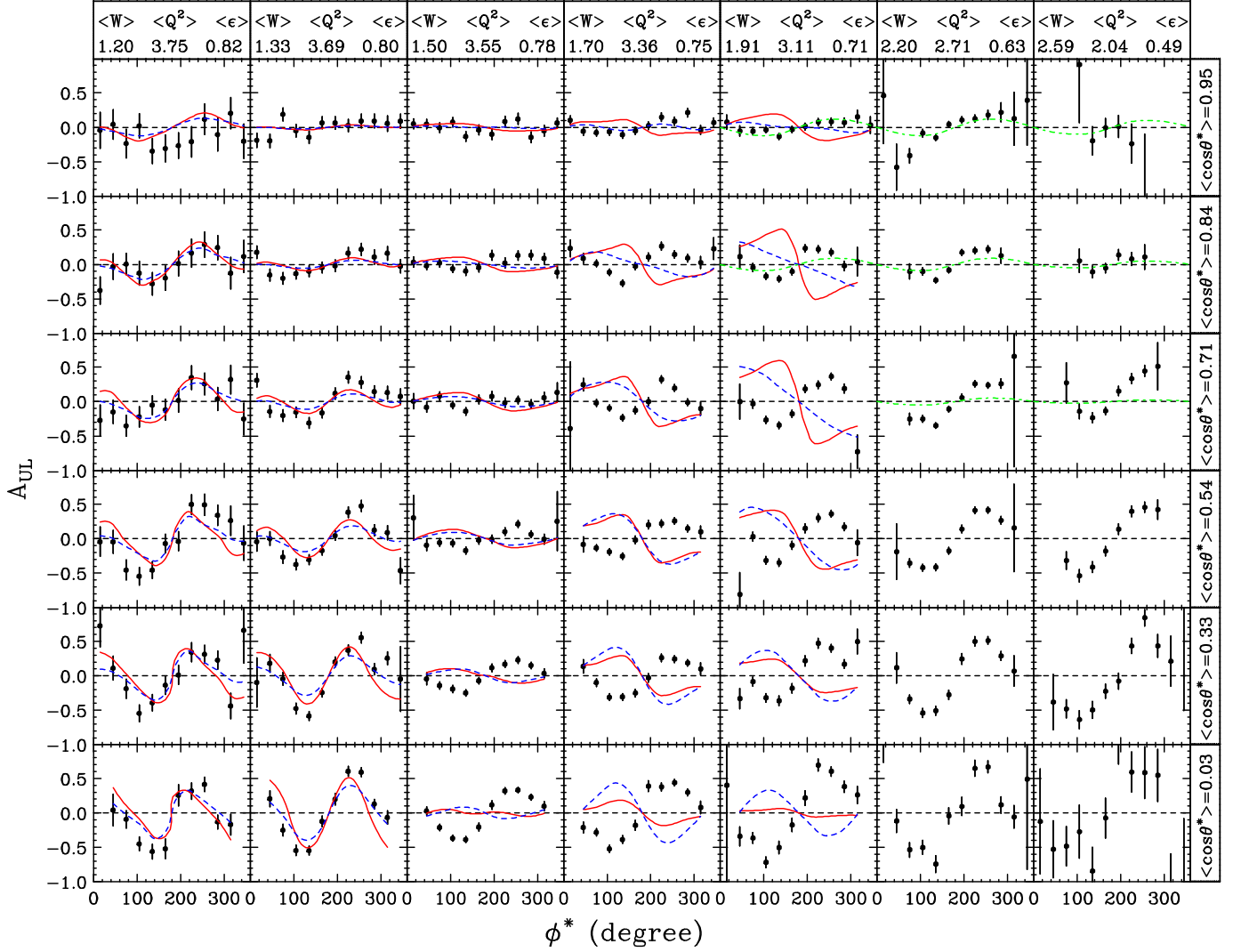


FIG. 11: Same as Fig. 10, except for the two larger Q^2 bins of this analysis.

Acknowledgments

We thank I. Aznauryan for providing the JANR source code and L. Tiator for providing the MAID 2007 source code. We thank X. Zheng for suggesting the functional form of the dilution factor fit. We acknowledge the outstanding efforts of the staff of the Accelerator and the Physics Divisions at Jefferson Lab that made this experiment possible. This material is based upon work supported by the U.S. Department of Energy, Office of Science, Office

of Nuclear Physics under contract DE-AC05-06OR23177 and the National Science Foundation. Partial support was provided by the Scottish Universities Physics Alliance (SUPA), the United Kingdom’s Science and Technology Facilities Council, the National Research Foundation of Korea, the Italian Istituto Nazionale di Fisica Nucleare, the French Centre National de la Recherche Scientifique, and the French Commissariat à l’Energie Atomique. The Southeastern Universities Research Association (SURA) operates the Thomas Jefferson National Accelerator Facility for the United States Department of Energy under contract DE-AC05-84ER-40150.

-
- [1] C. J. Bebek *et al.*, Phys. Rev. D **13**, 25 (1976).
 - [2] C. J. Bebek *et al.*, Phys. Rev. D **17**, 1693 (1978).
 - [3] T. Horn *et al.*, Phys. Rev. C **78**, 058201 (2008).
 - [4] H. P. Blok *et al.*, Phys. Rev. C **78**, 045202 (2008).
 - [5] X. Qian *et al.*, Phys. Rev. C **81**, 055209 (2010).
 - [6] H. Egiyan *et al.* (CLAS Collaboration), Phys. Rev. C **73**, 025204 (2006); K. Park *et al.*, (CLAS Collaboration), Phys. Rev. C **77**, 015208 (2008).
 - [7] K. Park *et al.* (CLAS Collaboration), Phys. Rev. C **91**, 045203 (2015).
 - [8] K. Park *et al.* (CLAS Collaboration), Eur. Phys. J. A **49**, 16 (2013).
 - [9] J. C. Collins, L. Frankfurt, and M. Strikman, Phys. Rev. D **56**, 2982 (1997).
 - [10] S. V. Goloskokov and P. Kroll, Eur. Phys. J. C **65**, 137 (2010); S. V. Goloskokov and P. Kroll, Eur. Phys. J. A **47**, 112 (2011).
 - [11] H. Avakian *et al.*, Phys. Rev. D **69** (2004) 112004.
 - [12] R. De Vita *et al.* (CLAS Collaboration), Phys. Rev. Lett. **88**, 082001 (2002).
 - [13] P. E. Bosted *et al.* (CLAS Collaboration), arXiv:1604.04350 [nucl-ex], submitted to Phys. Rev. C.
 - [14] www.portal.kph.uni-mainz.de/MAID/; D. Drechsel, O. Hanstein, S.S. Kamalov, L. Tiator, Nucl. Phys. **A645**, 145 (1999).
 - [15] Y. Prok *et al.* (CLAS Collaboration), Phys. Rev. C **90** (2014) 2,025212.
 - [16] E. Seder *et al.* (CLAS Collaboration), Phys. Rev. Lett. **114**, 032001 (2015); S. Pisano *et al.* (CLAS Collaboration), Phys. Rev. D **91**, 052014 (2015).

- [17] C.D. Keith *et al.*, Nucl. Instr. Meth. **501**, 327 (2003).
- [18] B.A. Mecking *et al.*, Nucl. Instr. Meth., **503**, 513 (2003).
- [19] R.G. Fersch, *et al.* (CLAS Collaboration), to be published.
- [20] N. Guler *et al.* (CLAS Collaboration) , Phys. Rev. C **92**, 055201 (2015).
- [21] Y. S. Tsai, Report No. SLAC-PUB-848 (1971); Y. S. Tsai, Rev. Mod. Phys. 46, 815 (1974).
- [22] <http://clas.sinp.msu.ru/cgi-bin/jlab/db.cgi>
- [23] See Supplemental Material at [URL will be inserted by publisher] for plain text tables of asymmetry results for this experiment.
- [24] I. G. Aznauryan, Phys. Rev. C **67**, 015209 (2003); I. G. Aznauryan *et al.* (CLAS Collaboration), Phys. Rev. C **80**, 055203 (2009).
- [25] K.A. Olive *et al.* (Particle Data Group)], Chin. Phys. C **38**, 090001 (2014) and 2015 update.